VOLCANIC PLUMES

# The January 2022 eruption of Hunga Tonga-Hunga Ha'apai volcano reached the mesosphere

Simon R. Proud[1,2]*, Andrew T. Prata[2], Simeon Schmauß[3]

**Explosive volcanic eruptions can loft ash, gases, and water into the stratosphere, which affects both human activities and the climate. Using geostationary satellite images of the 15 January 2022 eruption of the Hunga Tonga-Hunga Ha'apai volcano, we find that the volcanic plume produced by this volcano reached an altitude of 57 kilometers at its highest extent. This places the plume in the lower mesosphere and provides observational evidence of a volcanic eruption injecting material through the stratosphere and directly into the mesosphere. We then discuss potential implications of this injection and suggest that the altitude reached by plumes from previous eruptions, such as the eruption of Mount Pinatubo in 1991, may have been underestimated because of a lack of observational data.**

Large explosive volcanic eruptions are important because they can affect climate (*1*), disrupt aviation (*2*), and pose numerous hazards to communities living nearby (*3*, *4*). The degree to which explosive volcanic eruptions affect climate is largely dependent on the volcano's latitude, the plume height, and the amount of $SO_2$ gas that is released (*5*). When a substantial amount of $SO_2$ is released into the atmosphere, it is converted to sulfate aerosols that can, in the most extreme cases, persist for several years (*6*), and when injected at low latitudes, the aerosol disperses into both hemispheres (*1*, *7*). The persistent aerosol veil that is produced affects climate because of the reflection of incoming visible radiation and absorption of near-infrared radiation (*8*), which results in a cooling of the troposphere (*9*) and heating of the stratosphere (*10*). Within the satellite era, there are numerous examples of volcanic plumes reaching the upper troposphere–lower stratosphere (*11*); however, few have been observed to reach higher than 30 km and affect the climate (*12*). Notable examples that have been observed and quantified using satellite observations include the plumes of Mount Pinatubo (Philippines) in 1991, which injected ~20 Tg of $SO_2$ (*13*) and reached 40 km at its highest point (*14*), and El Chichón, which released ~7.5 Tg of $SO_2$ into the atmosphere (*15*) in 1982, reaching 31 km (*16*). Based on the satellite data record, in general, individual explosive volcanic eruptions are not expected to have a measurable climate impact unless >1 Tg $SO_2$ is released into the stratosphere (*12*).

The Hunga Tonga-Hunga Ha'apai (HTHH) volcano (20.536°S, 175.382°W) is an underwater caldera volcano located ~70 km north-northwest of Tonga's capital, Nukualofa. Recent Surtseyan-style eruptive activity was observed in 2009, from 2014 to 2015, and from 20 December 2021 to 15 January 2022 (*17*). In the lead-up to the 15 January 2022 eruption, described later in the text, a large phreatomagmatic eruption, similar to the December 2019 eruption of Anak Krakatau, Indonesia (*18*), was observed on 13 January in geostationary satellite data. The volcanological setting of HTHH is very different from those of the Mount Pinatubo and El Chichón volcanoes because of the abundance of seawater available for magma interaction. Initial estimates of the total mass of $SO_2$ released by the 15 January eruption from hyperspectral sounders and ultraviolet instruments were 0.2 to 0.4 Tg $SO_2$ (*19*, *20*). This amount of $SO_2$ is low and suggests that large amounts of $SO_2$ may have been scavenged through wet deposition (*18*, *21*).

On 15 January 2022, at about 04:06 UTC (17:06 local time), the HTHH volcano violently erupted, producing the large volcanic plume shown in Fig. 1. A second smaller eruption occurred at 08:00 UTC, with no further large eruptions occurring thereafter. This eruption was one of the most powerful in recent years, triggering a tsunami that was felt across the Pacific and atmospheric waves (*22*) that circled Earth multiple times, which were seen as fluctuations in global pressure sensor readings for several days. The volcano's location is well covered by satellite sensors, with three geostationary weather satellite platforms providing imagery of the area at visible and infrared

[1]National Centre for Earth Observation, RAL Space, STFC Rutherford Appleton Laboratory, Harwell OX11, UK. [2]Atmospheric, Oceanic and Planetary Physics, University of Oxford, Parks Road, Oxford OX1 3PU, UK. [3]Munich University of Applied Sciences, Lothstraße. 34, 80335 Munich, Germany.
*Corresponding author. Email: simon.proud@stfc.ac.uk

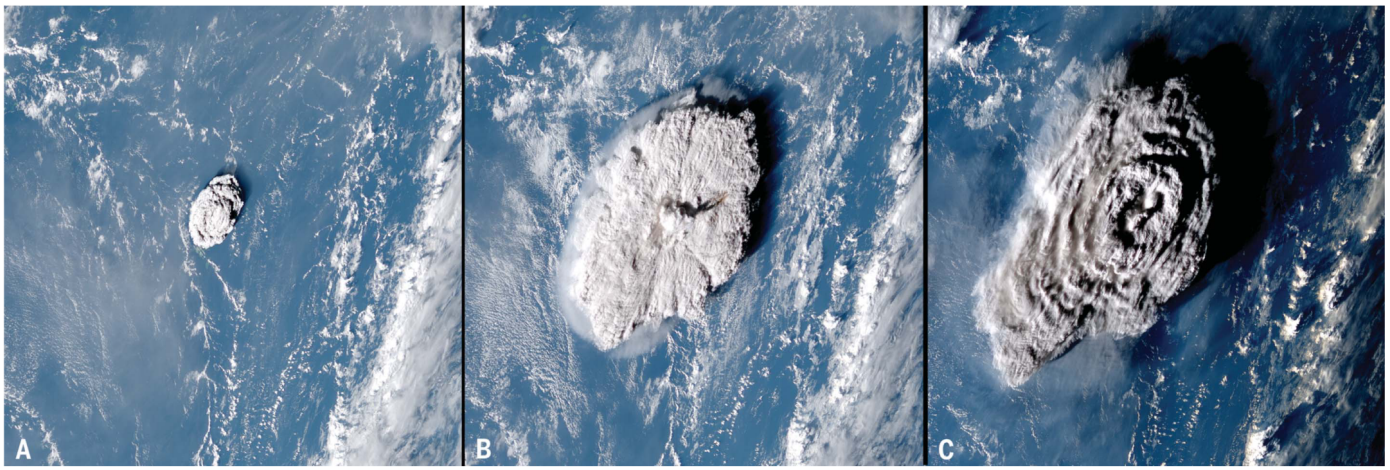


**Fig. 1. The HTHH eruption as viewed from the Himawari-8 weather satellite.** (**A**) At 04:20 UTC on 15 January 2022, ~10 min after the eruption began. (**B**) At 04:50 UTC, after the initial dome collapsed, leaving remnants at 55- to 58-km altitude that cast a shadow (to the right) onto the umbrella cloud at 34 km. (**C**) At 05:40 UTC, as the volcanic umbrella spreads south-westward and the Sun begins to set, emphasizing the shadows that we used to calculate plume altitude and highlighting wave structure in the umbrella top.

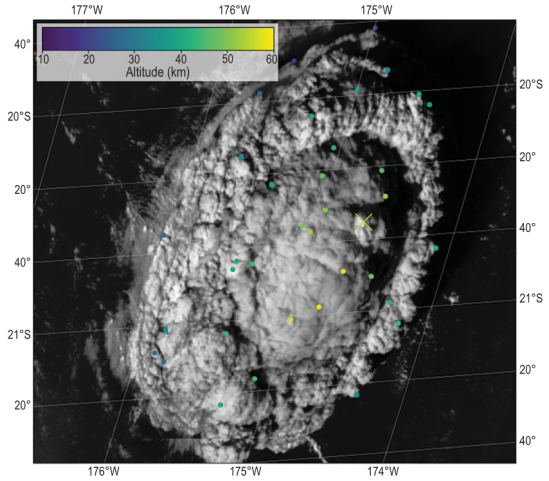


**Fig. 2. Parallax-based retrievals of plume altitude at 04:30 UTC on 15 January 2022 overlaid on Himawari-8 high-resolution data for the same time frame.** Colored circles represent Advanced Himawari Imager (AHI)–Advanced Meteorological Imager (AMI) retrievals, and the two crosses represent AHI-AMI–Advanced Baseline Imager (ABI) retrievals.

wavelengths every 10 min (summarized in table S1), and at about 07:05 UTC, the National Oceanic and Atmospheric Administration (NOAA) enabled a fast-scanning mesoscale sector over the volcano, producing imagery every minute.

Typically, the altitude of a volcanic plume is estimated from its top temperature measured by satellite and compared with a vertical profile of temperature from radiosonde measurements or weather model outputs such as those produced by the European Centre for Medium-Range Weather Forecasts (ECMWF) (*23*). This technique makes use of the relationship between decreasing atmospheric temperature—and hence cloud temperature for a cloud in thermodynamic equilibrium with its surroundings—and altitude in the troposphere (*24*). However, for large volcanic eruptions, the cloud penetrates the tropopause and enters the stratosphere, where temperature increases with altitude, thus rendering temperature-based techniques inaccurate: In such cases, the plume in the stratosphere will initially be cooler than the ambient air but will warm as the plume enters thermodynamic equilibrium with its surroundings, which presents several possible altitude solutions for a single cloud temperature. This is further complicated because the eruption itself is likely to affect local vertical temperature profiles. In this report, we make use of the multiple satellite sensors that viewed the eruption from very different viewing geometries to compute plume altitude based on the parallax effect, which does not suffer from the limitations described earlier in the text, and find that the HTHH eruption not only penetrated the stratosphere but also reached the lower mesosphere.

When a satellite views a high-altitude cloud, the cloud location within the satellite image will be incorrect because of a parallax shift, the magnitude of which depends on the viewing angle between satellite and cloud and upon the cloud altitude. If two or more satellites view a cloud from differing locations, then its actual position and altitude are found by iteratively adjusting estimated cloud altitude to minimize the difference in the parallax-corrected position between satellites (*25*). We have previously used this approach to successfully estimate the altitude and trajectory of the Chelyabinsk meteor (*26*), demonstrating that the technique is appropriate for high-altitude clouds. Here, we apply the approach to a series of manually selected cloud positions observed by Himawari-8 and GEO-KOMPSAT-2A (GK-2A) to the west of the eruption and the Geostationary Operational Environmental Satellite (GOES-17) to the east across images taken between 04:16 and 06:36 UTC, after which the Sun set. In addition, we perform a more detailed analysis of the 04:36 UTC imagery from Himawari-8 and GK-2A to map variations in altitude across the plume, which is shown in Fig. 2. Because these methods rely on manual point selection and analysis, they cannot map altitude across the whole plume. To gain a broad perspective of plume altitude, we therefore also applied a stereoscopic vision tool to estimate altitude, which is less accurate but can provide spatial information, and the standard temperature-based

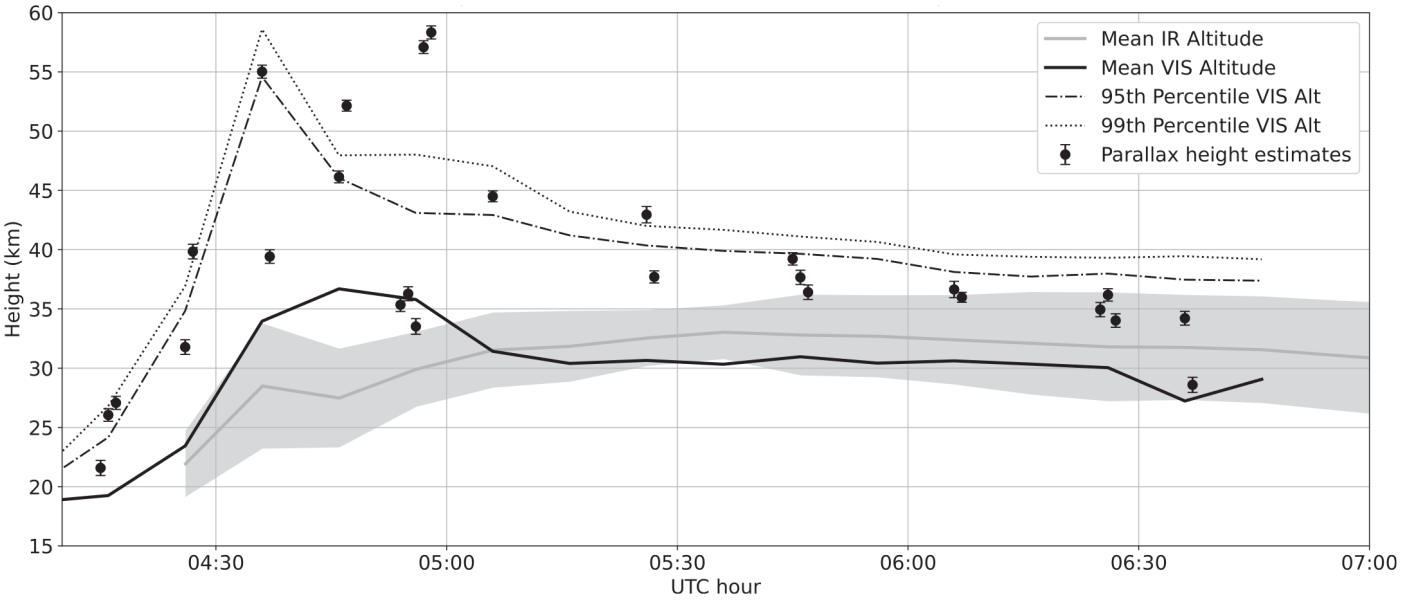


**Fig. 3. Temporal evolution of volcanic plume altitude derived from visible and infrared data.** Infrared (IR) heights are derived from Himawari-8 brightness temperature measurements and the ECMWF temperature profile. The gray-shaded area represents one standard deviation from the mean. The blue lines indicate altitudes estimated by the stereoscopic method applied to VIS (visible) data across the entire volcanic plume, and the green markers are parallax heights derived from a manual analysis of data from Himawari-8, GK-2A, and GOES-17. Error bars show the spread of estimated altitudes due to simulated geolocation uncertainty. Because of sunset, no visible altitudes are available after 06:46 UTC. All times given are for 15 January 2022.

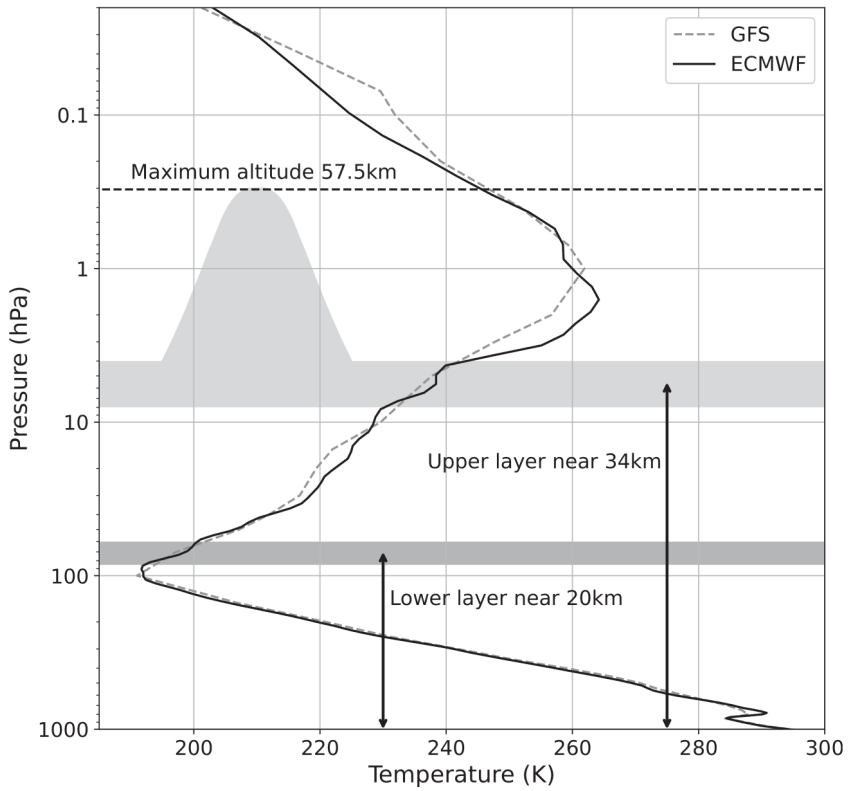


**Fig. 4. Vertical structure of the volcanic plume.** Represented are a lower near-tropopause layer, the altitude of which cannot be accurately determined; the main umbrella at higher altitude; and the dome-like protrusion seen in the 04:30 UTC satellite images from 15 January 2022. Layer thickness is computed from the spread of parallax-based altitude retrievals for each layer and, when optically thick, by using the infrared brightness temperature approach. Overlaid are the 00:00 UTC Global Forecast System (GFS) and ECMWF temperature profiles that show the tropopause near 100 hPa and the stratopause between 1 and 1.5 hPa.

retrieval described earlier in the text. The results of all three techniques are shown in Fig. 3. Further information on the methods used here, including tables of parallax-retrieved altitudes, is given in the supplementary materials.

Altitude retrievals from the early phase of the eruption show a rapidly ascending plume that reached 25 km about 15 min after the eruption began and 40 km, in the upper stratosphere, after 25 min. By 04:36 UTC, a half hour after the eruption began, a dome, ~90 km in diameter, was visible that extended from 34 km up to 57 km altitude (~0.3 hPa in the ECMWF analysis), which is 13 km above the local stratopause (1.5 hPa)—well within the mesosphere. We estimate the uncertainty on this altitude to be less than 1.5 km. Encircling this dome was a donut-shaped structure with altitudes peaking at 41 km (2.2 hPa) and a secondary layer just above the ECMWF tropopause at 17.5 km (91 hPa). A schematic of the eruption at this point is shown in Fig. 4. Ten minutes later, the dome collapsed to leave the expanding donut cloud, although the haziness visible in the central region above the volcano indicates that high-altitude aerosols such as sulfates or ash are likely to be present. This haze is too optically thin, though, to support altitude retrieval. By 04:56 UTC, the eruption had produced a vertical column stretching from the surface to the mesosphere, including two tendrils that reached 58 km (0.28 hPa). These tendrils cast a shadow onto the remaining volcanic cloud at 35-km altitude, and calculating tendril altitude from the shadow length gives an altitude of 57.5 km, which closely matches the parallax-derived altitude. Thereafter, as shown in Fig. 3, peak altitude decreased, and no further mesospheric intrusions were detected. Analysis of the infrared imagery shows two clouds over the next 12 hours: One moving south-west in the prevailing winds at 30 to 35 km altitude and one moving east at the tropopause.

The influence of volcanoes on the mesosphere is unclear. Previous eruptions into the stratosphere have indirectly affected the mesosphere through the upward-ascent transport of volcanic aerosols after an eruption (*27*), although the chemical processes acting on mesospheric volcanic aerosols are the subject of debate (*28*). Vertical propagation of gravity waves from volcanoes can affect the mesospheric temperature (*29*), whereas the aerosols and water vapor injected to high altitude by the 1883 Krakatoa eruption may have been responsible for subsequent apparent increases in mesospheric clouds. However, there is no agreement as to why some volcanic eruptions but not others are associated with mesospheric cloud increases (*30*). Our observations of the HTHH plume provide direct evidence that volcanic eruptions can inject material into the mesosphere and will enable a more detailed analysis of mesospheric chemistry and transport.

However, our work also raises questions: What mechanisms contributed to this eruption reaching such high altitude but with little $SO_2$ being observed? What is the composition of the hazy substance that is visible atop the highest portions of the plume, and how long will it persist in the mesosphere? In addition, we show that the mesospheric altitudes achieved by this plume were only visible in satellite images taken at two times (those starting at 04:30 and 04:50 UTC), highlighting the importance of frequent, every 10 min in this case, satellite observations. Previous eruptions were observed much less frequently by satellite, once every hour by only one satellite (GMS-4) in the case of Mount Pinatubo, meaning that the peak altitude reached by the volcanic plume is likely to have fallen between observations and that parallax-based height estimates were not possible. If the 2022 HTHH eruption had been observed by the same satellite as that in the case of Mount Pinatubo, the peak altitudes observed would have been substantially lower than those described here: 32 km per infrared data and 39 km using the shadow technique used for Mount Pinatubo (*14*).

## REFERENCES AND NOTES


1. A. Robock, *Rev. Geophys.* **38**, 191–219 (2000).
2. T. J. Casadevall, Ed., "Volcanic ash and aviation safety: Proceedings of the first international symposium on volcanic ash and aviation safety" (US Geological Survey Bulletin 2047, US Government Printing Office, 1994).
3. S. C. Loughlin, S. Sparks, S. K. Brown, S. F. Jenkins, C. Vye-Brown, Eds., *Global Volcanic Hazards and Risk* (Cambridge Univ. Press, 2015).
4. T. M. Wilson, S. Jenkins, C. Stewart, in *Volcanic Hazards, Risks and Disasters*, J. F. Shroder, P. Papale, Eds. (Elsevier, 2015), pp. 47–86.
5. C. Schnetzler, G. Bluth, A. Krueger, L. Walter, *J. Geophys. Res.* **102**, 20087–20091 (1997).
6. S. Kremser *et al.*, *Rev. Geophys.* **54**, 278–335 (2016).
7. J. Hansen, A. Lacis, R. Ruedy, M. Sato, *Geophys. Res. Lett.* **19**, 215–218 (1992).
8. G. L. Stenchikov *et al.*, *J. Geophys. Res.* **103**, 13837–13857 (1998).
9. E. G. Dutton, J. R. Christy, *Geophys. Res. Lett.* **19**, 2313–2316 (1992).
10. K. Labitzke, M. P. McCormick, *Geophys. Res. Lett.* **19**, 207–210 (1992).
11. A. Bernard, W. I. Rose Jr., *Nat. Hazards* **3**, 59–67 (1990).
12. S. Carn, L. Clarisse, A. Prata, *J. Volcanol. Geotherm. Res.* **311**, 99–134 (2016).
13. S. Guo, G. J. Bluth, W. I. Rose, I. M. Watson, A. Prata, *Geochem. Geophys. Geosyst.* **5**, Q04001 (2004).
14. R. E. Holasek, S. Self, A. W. Woods, *J. Geophys. Res.* **101**, 27635–27655 (1996).
15. A. Krueger, N. Krotkov, S. Carn, *J. Volcanol. Geotherm. Res.* **175**, 408–414 (2008).
16. M. Matson, *J. Volcanol. Geotherm. Res.* **23**, 1–10 (1984).

17. M. Brenna *et al.*, *Lithos* **412-413**, 106614 (2022).
18. A. T. Prata *et al.*, *Sci. Rep.* **10**, 3584 (2020).
19. Global Volcanism Program, in vol. 47 of the *Bulletin of the Global Volcanism Network*, A. E. Crafford, E. Venzke, Eds. (Smithsonian Institution, 2022).
20. M. Zuo *et al.*, *Adv. Atmos. Sci.* 10.1007/s00376-022-2034-1 (2022).
21. W. I. Rose *et al.*, *Nature* **375**, 477–479 (1995).
22. D. A. Yuen *et al.*, *Earthquake Research Advances* **2**, 100134 (2022).
23. R. G. Owens, T. Hewson, "ECMWF forecast user guide" (European Centre for Medium-Range Weather Forecasts, 2018).
24. C. Oppenheimer, *Int. J. Remote Sens.* **19**, 2829–2864 (1998).
25. L. Merucci, K. Zakšek, E. Carboni, S. Corradini, *Remote Sens.* **8**, 206 (2016).
26. S. Proud, *Geophys. Res. Lett.* **40**, 3351–3355 (2013).
27. M. J. Mills, O. B. Toon, G. E. Thomas, *J. Geophys. Res. D Atmospheres* **110**, D24208 (2005).
28. C. George *et al.*, in *Atmospheric and Aerosol Chemistry*, V. McNeill, P. Ariya, Eds. (Topics in Current Chemistry 339, Springer, 2012), pp. 1–53.
29. C. von Savigny *et al.*, *Meteorol. Z.* **29**, 3–18 (2020).
30. C. Bertolin, F. Domınguez-Castro, *Holocene* **30**, 682–690 (2020).

## ACKNOWLEDGMENTS

We thank J. Amos for the initial recognition that this eruption reached the mesosphere and acknowledge helpful discussions with E. Carboni and R. Grainger regarding the HTHH eruption and drafts of this paper. We also acknowledge the NOAA's Big Data Program for making GFS, GOES-17, and Himawari-8 data openly accessible; the Japan Meteorological Agency for its Himawari-8 data access; and the Korea Meteorological Administration (KMA) for making GEO-KOMPSAT-2A data available via its open application programming interface (API). We also thank the ECMWF for provision of the temperature vertical profile analysis used in this study. **Funding:** S.R.P.'s work on this study was funded as part of NERC's support of the National Centre for Earth Observation, award ref. NE/R016518/1; and by a NERC Innovation fellowship, award ref. NE/R013144/1. A.T.P. was funded by NERC's support of the Radar-supported Next-Generation Forecasting of Volcanic Ash Hazard project, award ref. NE/S003843/1. **Author contributions:** S.R.P. formulated the research, wrote the parallax and infrared retrieval code, and analyzed the results. A.T.P. also analyzed the results, and both S.R.P. and A.T.P. contributed to drafting the manuscript. S.S. devised and performed the stereoscopic height retrievals. **Competing interests:** The authors declare no competing interests. **Data and materials availability:** GOES-16 and Himawari-8 satellite data are available through NOAA's Big Data Program: https://www.noaa.gov/nodd/datasets. GK-2A data are available via KMA's open data API: https://datasvc.nmsc.kma.go.kr/. ECMWF and GFS profile data (filename TProfs.csv) and the Python code used to perform this analysis are available on GitHub: https://github.com/simonrp84/Tonga_Volcano_Code. The lists of points used for tri- and dual-satellite parallax calculations are also on the same GitHub page (filenames Points_Dual.csv and Points_Tri.csv). The infrared and stereoscopic retrieval outputs are in the Height_Out and Heightmap subdirectories, respectively. 

## SUPPLEMENTARY MATERIALS

science.org/doi/10.1126/science.abo4076
Materials and Methods
Table S1
References (*31*–*38*)

Submitted 1 February 2022; accepted 8 October 2022
10.1126/science.abo4076